The Astrophysical Journal, 972:110 (14pp), 2024 September 1 https://doi.org/10.3847/1538-4357/ad5ce3

Magnetic Eruption from a Three-ribbon Flare

Ju Jing, Jeongwoo Lee, Mia Mancuso, Qin Li, Nian Liu, Satoshi Inoue, Yan Xu, and Haimin Wang
Institute for Space Weather Sciences, New Jersey Institute of Technology, University Heights, Newark, NJ 07102-1982, USA; ju.jing@njit.edu

Received 2024 March 5; revised 2024 June 20; accepted 2024 June 26; published 2024 August 28

Abstract

We present observations and analysis of an eruptive M1.5 flare (SOL2014-08-01T18:13) in NOAA active region (AR) 12127, characterized by three flare ribbons, a confined filament between ribbons, and rotating sunspot motions as observed by the Solar Dynamics Observatory. The potential field extrapolation model shows a magnetic topology involving two intersecting quasi-separatrix layers (QSLs) forming a hyperbolic flux tube (HFT), which constitutes the fishbone structure for the three-ribbon flare. Two of the three ribbons show separation from each other, and the third ribbon is rather stationary at the QSL footpoints. The nonlinear force-free field extrapolation model implies the presence of a magnetic flux rope (MFR) structure between the two separating ribbons, which was unclear in the observation. This suggests that the standard reconnection scenario for eruptive flares applies to the two ribbons, and the QSL reconnection for the third ribbon. We find rotational flows around the sunspot, which may have caused the eruption by weakening the downward magnetic tension of the MFR. The confined filament is located in the region of relatively strong strapping field. The HFT topology and the accumulation of reconnected magnetic flux in the HFT may play a role in holding it from eruption. This eruption scenario differs from the one typically known for circular ribbon flares, which is mainly driven by a successful inside-out eruption of filaments. Our results demonstrate the diversity of solar magnetic eruption paths that arises from the complexity of the magnetic configuration.

Unified Astronomy Thesaurus concepts: Solar filaments (1495); Solar flares (1496); Solar magnetic fields (1503)

1. Introduction

Solar flares and filament eruptions are signatures on the Sun's surface that often indicate the origin of coronal mass ejections (CMEs). Among them, the filament mass is often observed as the core of the early stage of a CME, while the flare is thought to be the two-dimensional (2D) projection of coronal magnetic reconnection on the solar surface. Thus, the morphology and dynamic behavior of flares provide clues to magnetic topology and physical processes of coronal magnetic reconnection.

Two-ribbon flares are the best-known type of solar flares, during which two parallel ribbons appear on either side of the magnetic polarity inversion line (PIL) and separate from each other in the direction perpendicular to the PIL as the flare progresses. The standard 2D reconnection model, established by Carmichael (1964), Sturrock (1966), Hirayama (1974), and Kopp & Pneuman (1976), can well explain the formation of such two ribbons by stacking the 2D X-point reconnection along the third dimension. In reality, however, solar flares occur in three-dimensional (3D) magnetic structure, and the resulting flare ribbons come in various forms more complex than the two parallel ribbons, including circular shape (Reid et al. 2012; Wang & Liu 2012; Masson et al. 2017; Zhong et al. 2019; Lee et al. 2020; Liu et al. 2020), X-shape (Liu et al. 2016a; Li et al. 2016), or multiple ribbons (Mandrini et al. 2014; Wang et al. 2014; Bamba et al. 2017; Zhong et al. 2019; Qiu et al. 2020) along with the increased degrees of freedom in the reconnecting dynamics (Lee 2022). The concept of quasi-separatrix layers (QSLs) was introduced for 3D magnetic structure where no magnetic reconnection can occur in the strict sense of ideal magnetohydrodynamics (MHD), and the reconnection should be facilitated via nonideal effects (Priest & Démoulin 1995; Demoulin et al. 1997; Titov et al. 2002; Aulanier et al. 2005; Longcope 2005).

QSLs are defined as regions where magnetic field connectivity has a very sharp gradient but is not as strictly discontinuous as in the case of separatrix surfaces (Priest & Démoulin 1995). QSLs can be recognized as thin volumes with high squashing factor Q ($\gg 1$, Titov et al. 2002), whereas the separatrix surfaces are defined by $Q \sim \infty$. Together with separatrix surfaces, QSLs form the skeleton of the magnetic field. Two separatrix surfaces intersect at a separator (the line of X-points in 3D); while when two QSLs intersect, they often take on an X-shaped cross section called a hyperbolic flux tube (HFT; Titov et al. 2002, 2003), which becomes a separator in the case where the QSL thickness reaches infinitesimal. Due to the strong distortion of magnetic mapping, QSLs and HFTs are preferred sites for electric current sheet development and magnetic reconnection (Effenberger et al. 2011; Craig & Effenberger 2014). Magnetic reconnection within QSLs, known as slipping or slip-running reconnection (Aulanier et al. 2006), manifests itself in observations as sequential brightening along the QSL footpoints at the chromosphere, which is often seen in circular ribbon flares. Not only can an HFT promote an eruption, it can also shred the ascending filament trying to pass through it and cause the eruption to fail (Chintzoglou et al. 2017).

Using the concept of QSLs we can accommodate the diversity of flare morphology and connectivity changes, which becomes an increasingly common practice in flare studies. As a special type of flares, circular ribbon flares have recently received increasing attention. They are hosted in a spine-fan magnetic topology, where the spine field passing through the null point diverges out at the null point to form the fan surface (i.e., the dome-shaped QSL), and the circular ribbon maps out the intersection of the QSL dome with the chromosphere (Masson et al. 2009; Reid et al. 2012; Sun et al. 2013; Xu et al. 2017; Mitra et al. 2023). Recently, some cases of flares consisting of both parallel and circular ribbons have also been reported (Joshi et al. 2017; Zhong et al. 2019; Joshi et al. 2021). In particular, Zhong et al. (2019) studied the transformation of a circular ribbon into parallel ribbons during a flare and pointed out that the bifurcation of the magnetic flux rope (MFR) is the main factor leading to this transformation. Lee et al. (2020) also reported subtle changes in a circular ribbon flare in which parallel ribbons form. These works highlight the complexity of 3D reconnections and pose new challenges in understanding the evolution of flares and 3D magnetic reconnections.

In addition to two-ribbon and circular ribbon flares, multi-ribbon flares are also commonly taking place, although much less studied. In particular, Wang et al. (2014) reported two sets of three-ribbon flares observed with the high-resolution Goode Solar Telescope (GST; Goode & Cao 2012) in Hα and with Hinode in Ca II H, respectively, both of which show three compact ribbons parallel to the PIL. They speculated that the 3D magnetic structure of the three-ribbon flares is a spine-fan magnetic field extending along the third dimension, as if the cross section of the spine-fan magnetic field topology were stacked in a 2.5D axisymmetric manner, forming an intriguing fishbone-like structure to accommodate the three-ribbon flares (see their Figure 5). Although other studies of three-ribbon flares show the complexity and variability of their magnetic field configuration (e.g., Bamba et al. 2017; Zhong et al. 2019; Qiu et al. 2020), the fishbone structure is the common basis for their formation and deserves further analysis.

This paper presents a detailed study of the 3D magnetic configuration of a three-ribbon flare, SOL2014-08-01T18:13. Unlike the compact three-ribbon flares reported by Wang et al. (2014), this three-ribbon flare occurred on a much larger scale with the outer two ribbons spanning ~200″. The full-disk vector magnetogram data from the Solar Dynamics Observatory (SDO; Pesnell et al. 2012) is well suited for our magnetic field study. Additionally, a large filament is located between two of the three ribbons, and well preserved during the flare, except a small strand erupting at the onset of the flare. The presence of a nonerupting filament amid this eruptive flare is another feature to be studied. The rest of the paper is organized as follows. We present our observations and analyses in Section 2, focusing on analyzing the 3D magnetic configurations and using the QSL method to aid in the analysis. Our results are discussed and summarized in Sections 3 and 4, respectively.

2. Observation and Analysis

We study the M1.5-class (SOL2014-08-01T18:13) flare that occurred in NOAA active region (AR) 12127 on 2014 August 1, associated with a halo CME. The flare emission in GOES soft X-ray (SXR) 1–8 Å flux starts at 17:55 UT, reaches a maxima at 18:13 UT, and ends at 18:48 UT. We use EUV 304 Å and 171 Å images obtained from the Atmospheric Image Assembly (AIA; Lemen et al. 2012) on board the SDO to study the flare morphology and associated coronal loop motions. Time series of SDO/AIA images in EUV passbands cover the solar disk at a pixel scale of 0.″6 and a cadence of 12 s.

2.1. Flare Ribbons and Eruption

Figures 1(a)–(d) show a series of AIA 304 Å images from the preflare to the later phase of the flare. The three flare ribbons are denoted by R1, R2, and R3, respectively. An animation of the flare observed in this passband is also provided in the online article. From the animation, we see that a pair of ribbons R1 and R2 first appears at approximately 17:58 UT, and a few minutes later (~18:02 UT), the third ribbon R3 appears, while R1 extends to the southwest and R2 to the southeast. The main parts of the three ribbons are parallel to each other, and R1's extension appears to be connected to R3, forming a quasi-semicircle. A large filament is located mainly between R2 and R3, which can be better recognized in the Hα image obtained by the Big Bear Solar Observatory (BBSO), as shown in Figure 1(e). Although the flare is eruptive. i.e., associated with a CME, the filament appears to be unaffected by the flare, with its body remaining largely in place after the flare. Figure 1(f) shows an AIA 171 Å image taken at the decay phase of the flare, from which the postflare loops between R1 and R2 are clearly visible, but the loops between R2 and R3 are not significant. This implies that the CME had originated from the eruption between R1 and R2.

We track the ribbon separation motion by placing a virtual slit, S1, shown in Figure 2(a), roughly perpendicular to the PIL, and then generate a distance–time stack plot along this slit, shown in Figure 2(b). It is clear that the R1/R2 pair exhibits an obvious separation motion, while R3 is almost stationary in that direction in time. Thus, in addition to the spatial offset, slight time delay, and lack of postflare loops, R3 also differs from the R1/R2 pair in its motion pattern. From this, we can infer that R1/R2 is a pair of primary flare ribbons, while R3 is a remote secondary ribbon.

Figure 2(c) shows the time profile of GOES SXR flux. Due to the absence of RHESSI hard X-ray data, we use the time derivative of SXR flux to represent the evolution of the nonthermal flare emission (Neupert 1968), which peaks at ~18:01 UT. In the standard flare reconnection model, the reconnecting magnetic flux in the corona can be related to the magnetic flux swept by the flare ribbons in the photosphere (Forbes & Priest 1984). We therefore measure the reconnecting flux using the techniques employed in some previous studies (e.g., Fletcher & Hudson 2001; Qiu et al. 2002, 2004, 2007; Jing et al. 2005; Saba et al. 2006; Lee & Gary 2008; Kazachenko et al. 2017), i.e., by summing the photospheric magnetic fluxes swept by the flare ribbons in SDO/AIA 1600 Å. The reconnection flux thus measured and the resulting reconnection rate are plotted in Figure 2(d). In general, the time profile of the reconnection rate is temporally correlated with that of nonthermal emission (see the two red curves in panels (c) and d), but the former reaches its peak approximately 2 minutes earlier than the latter. In other words, nonthermal electron acceleration is slightly delayed relative to magnetic reconnection. This time delay has also been noted in some magnetic reconnection studies (e.g., Sahu et al. 2020; Naus et al. 2022; Cannon et al. 2023), and the recent 3D MHD simulations have provided a physical explanation for this phenomenon; that is, the Fermi acceleration of nonthermal electrons is suppressed in the presence of strong conducting magnetic fields (Arnold et al. 2021; Dahlin et al. 2022).

Although the filament did not erupt, a rising feature near the eastern end of the filament is briefly captured in AIA 304 Å between 17:55 UT and 18:10 UT, which looks like a very small

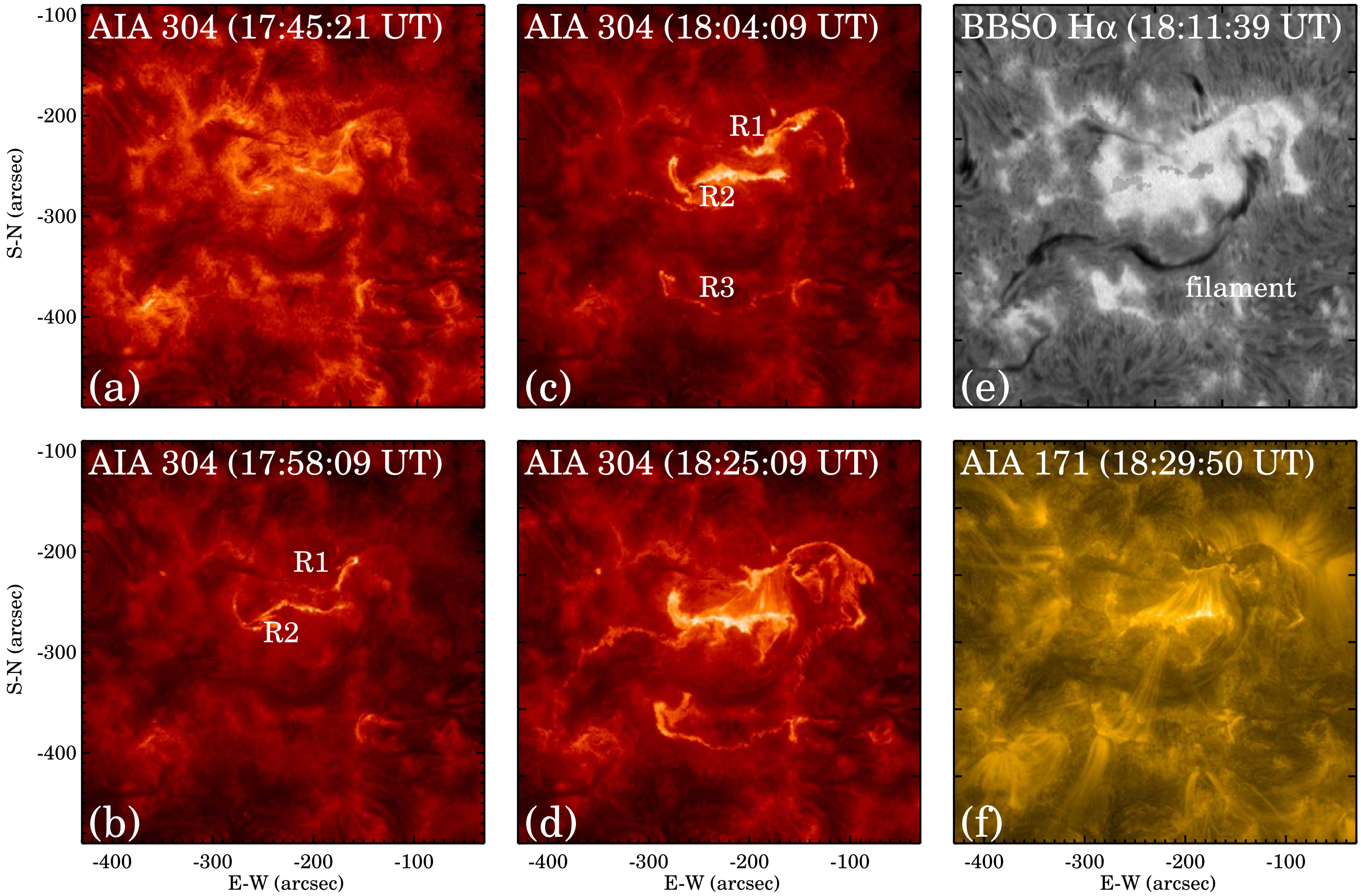

Figure 1. The three-ribbon flare observed by SDO/AIA and BBSO. (a) AIA 304 Å image taken before the flare. (b)–(d) AIA 304 Å images taken during the flare. A pair of ribbons R1 and R2 appear first, followed by the third ribbon R3. (e) BBSO Hα image taken during the flare, showing a filament between R2 and R3. (f) AIA 171 Å image at the decay phase of the flare, showing the postflare loops between R1 and R2. The flare observed in the AIA 304 Å passband is shown as an animation in the online journal. The duration of the animation is 8 s.

strand of filament mass ejects with the flare. We track its motion along the S2 direction, shown in Figure 2(e). This small eruption occurs essentially at the same time as the flare, and quickly becomes less visible and impossible to track.

The expansion of the coronal loops can also be seen in the distance–time stack plot of the AIA 171 Å image sequence. In Figure 3(a), two virtual slits S2' and S3 are placed to generate the distance–time stack plots, as shown in Figures 3(b) and (c), respectively, in which the position of S2' is slightly different from that of S2 in Figure 2(a) to better display the coronal loop motion in 171 Å. At the location of the small strand eruption observed with AIA 304 Å, AIA 171 Å also observes an expansion of coronal loops, one end of which is apparently anchored at the negative magnetic field near the east end of the filament, and the other end of which, although not clearly visible, should be connected to the positive field of R1. The expansion of the coronal loops starts about 10 minutes before the flare, and is relatively slow prior to the flare, and then rises at a faster rate after the flare onset, as marked by the dotted lines in Figure 3(b). Meanwhile, S3 tracks the apparent southward expansion of the coronal loops connecting the main ribbon pair R1 and R2, and their motion shows the same pattern, i.e., the relatively slow expansion of the coronal loops begins long before the flare (about 30 minutes), and the loops rise at a much faster rate instantly after the flare onset, as shown in Figure 3(c). The coronal loops between R1 and R2 rise slowly prior to the flare and move fast during the flare. This implies that the eruption was successful, although the overall eruption signature in this event is less obvious due to the absence of the rising filament.

2.2. Magnetic Field Configuration

We use photospheric magnetogram data obtained from the Heliospheric and Magnetic Imager (HMI; Schou et al. 2012) on the SDO to study the magnetic field of the flare. SDO/HMI takes full-disk vector magnetograms at $0\farcs5$ pix^{-1} and 120 s cadence.

To construct the 3D magnetic field, we first generate the preflare cylindrical equal area (CEA) map with the SDO/HMI magnetogram data at 17:36 UT and use the generated CEA map as the bottom boundary conditions for the 3D magnetic field extrapolation. The CEA map is generated in the same way as the standard HMI SHARP CEA data series but with a greatly expanded field of view (FOV). The resulting magnetic field map includes B_x, B_y, and B_z in the heliographic coordinates, with 340×340 pixels at a uniform spatial sampling of $3''$ pix^{-1}. Figure 4(a) shows the B_z map, whose large FOV encompasses not only the AR 12127 where the flare occurred, but also its neighboring ARs. The box in the middle shows the FOV of the flare observation in Figure 1. We sacrifice spatial sampling to some extent to achieve the large FOV. This is because the

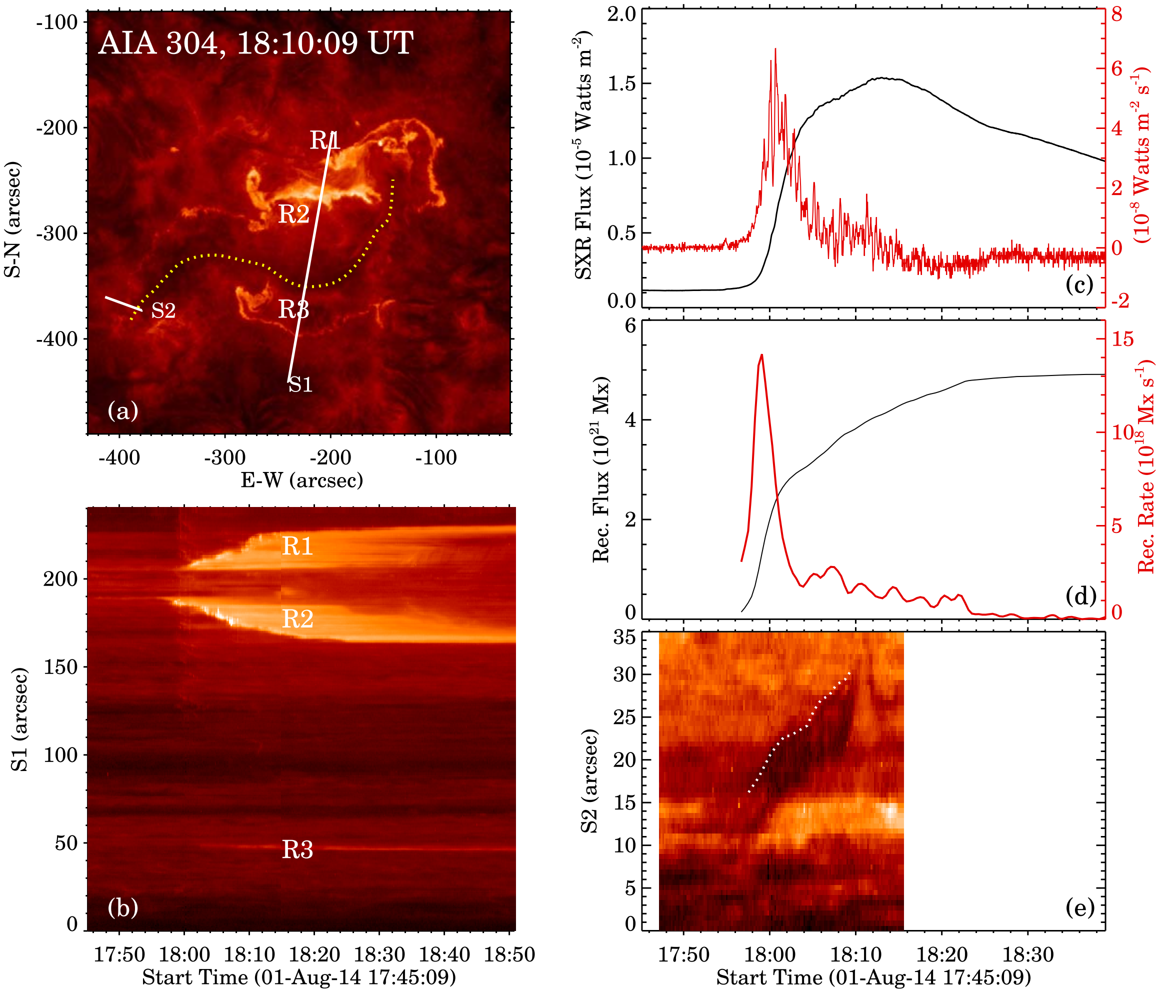

Figure 2. Overview of the three-ribbon flare and the associated eruption seen in the chromosphere. (a) The AIA 304 Å image taken at the impulsive phase of the flare shows three flare ribbons R1, R2, and R3. The dotted curve delineates the position of the filament located between R2 and R3. Two virtual slits, S1 and S2, were used to construct the distance–time stack plots displayed in (b) and (e), respectively. The end of the slits with the label "S1" and "S2" corresponds to the slit position "0." (b) Time–distance stack plot along S1 shows the separation motion of R1 and R2, as well as R3, which is stationary in the direction of S1. (c) GOES soft X-ray 1–8 Å flux (black) and its time derivative (red). (d) Measured magnetic flux reconnection rate (black) and its time derivative (red). (e) Time–distance stack plot along S2 shows the the rise of the eruption near the eastern end of the filament. The dotted line tracks the leading edge of the erupting feature.

reconstruction of the QSL structure needs to take into account the magnetic field line connectivity in all directions, which requires a large FOV.

We then extrapolate the potential field, using the Green's function method (Aly 1989), within a computational domain of $340 \times 340 \times 340$ uniform grid points (corresponding to $\sim 740 \times 740 \times 740$ Mm^3). The calculation of squashing factor Q is performed in the entire potential field domain, using the method of Liu et al. (2016b). We here use the potential field model rather than the more realistic nonlinear force-free (NLFF) field model because the potential field model allows easier identification of the connectivity, which is robust against the assumptions made in each extrapolation technique. Figure 4(b) shows the signed logarithmic Q factor (simply slog$Q$; see Titov et al. 2011) map at the photosphere. The so-called "signed" means that the sign of the slog$Q$ map is consistent with the polarity of the photospheric magnetic field, with positive values (red color) representing positive magnetic polarity and negative values (blue color) representing negative polarity. The magnetic field in the flare region (the boxed area in Figures 4(a) and (b)) is mainly a quadrupolar configuration composed of the magnetic fields of AR 12127 and AR 12131 and some dispersed magnetic fields to the south of AR 12131 outside the box area. Due to this quadrupole configuration, there are two QSLs whose footpoints in the slog$Q$ map are shown like two interconnected approximate circles, one large (blue) and one small (red), see Figure 4(b). AR 12130, on the other hand, is enclosed within a relatively isolated circular high-Q line. Figures 4(c) and (d) are enlarged views of the boxed areas in Figures 4(a) and (b), respectively. Combining these two panels, we see that the small red near-circular high-Q line connects the positive magnetic field of AR 12127 and the positive magnetic field of AR 12131, and this red high-Q line wraps the blue high-Q line connecting the negative magnetic fields of AR 12127 and AR 12131 in the middle, like a sandwich. The sandwiched blue high-Q line is actually part of a large blue circular high-Q line in the large FOV shown in Figure 4(b), which in turn wraps part of the small red circle in the middle. The small sandwich area is where the flare occurs and where the filament resides. The R1/R2 pair is located in one of the sandwich layers, the filament is located in the other, and R3 is highly coincident with the red high-Q line in the outer layer, see Figure 4(f). The spatial correlation between R3 and the high-Q line suggests that the presence of R3 is most

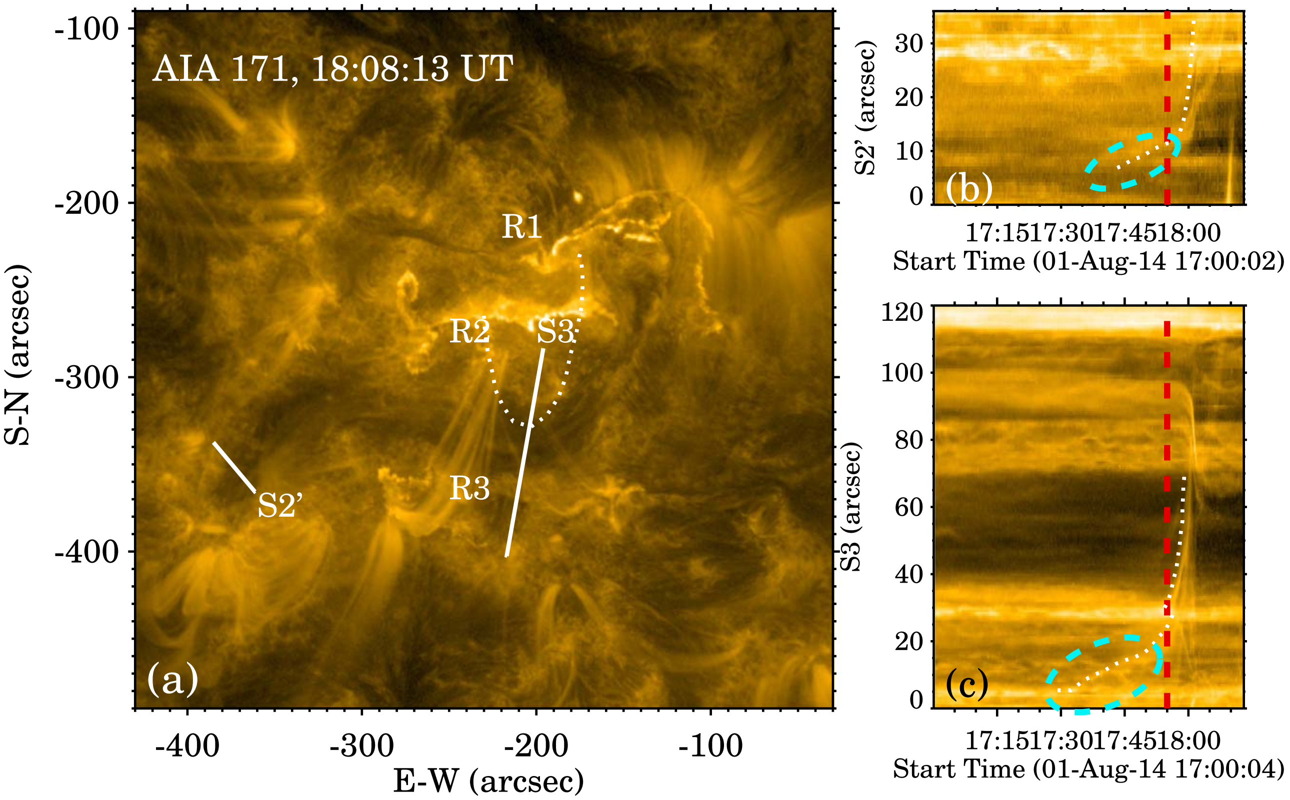

Figure 3. Eruption of coronal loops. (a) A snapshot of AIA 171 Å image showing three ribbons R1, R2, and R3, with the virtual slits S2' and S3 to generate the spacetime stack plots shown in (b) and (c), respectively. The end of the slit with the label "S3" corresponds to the slit position "0." The dotted curve connecting R1 and R2 delineates the shape of the rising coronal loops at 17:57:12 UT. (b), (c) Time–distance stack plots along S2' and S3, respectively. The vertical red dashed line marks the start time of the flare. The dotted lines track the trajectories of the erupting loops. The blue ellipse symbols highlight the slow upward motion prior to the flare. The flare and loop motion observed in this AIA passband is shown as an animation in the online journal. The duration of the animation is 10 s.

likely the result of slipping/slip-running reconnection along the corresponding QSL.

These high-Q circles or approximate circles shown on the photospheric surface are actually the footpoints of dome-shaped QSLs in three dimensions. Figure 5 exhibits the 3D distribution of the unsigned logarithm of Q factor ($\log Q$) over the entire FOV of the potential field with heights ranging from 0 to 150 Mm. "Unsigned" means that only the intensity of $\log Q$ is displayed, without distinguishing between positive and negative magnetic polarity, and 150 Mm is the approximate height of the largest QSL dome. To better visualize the QSL dome structure, we screen out the Q factors with logarithms less than 4 from the figure. In Figure 5, the overall 3D topology is comprised of three QSL domes; one above AR 12130, which is a typical spine-fan topology with a null point; the largest one above AR 12131; and the smallest and less structured one above the flare-producing AR 12127. Since the QSL dome of AR 12130 is relatively isolated, we ignore it in our analysis. The latter two domes intricately intersect each other in the corona, and we do not find any null points associated with them.

The intersection of two QSLs presents a volumetric structure with an X-shaped cross section, the HFT. Figure 6 shows a $\log Q$ vertical cross section across the two intersecting QSLs, from which we can clearly see this HFT structure. This structure subdivided the interior of the intersecting domes into three connectivity domains, a mid-arcade just below the X-shape, and two infra-arcades on each side of the mid-arcade (Chintzoglou et al. 2017). Figures 6(b) and (e) show the magnetic field lines under the domes, viewed from the top and from the east, respectively. The field lines are grouped by color according to their connectivity domains: the yellow infra-arcade connects R1 and R2; the cyan mid-arcade is closely related to the filament; and the gray infra-arcade, while not directly associated with the flare or the filament, is plotted to provide a full picture of the magnetic field lines under the QSL domes. Figures 6(c) and (f) show higher magnetic field lines that are approximately the same height as the two QSL domes. The red magnetic field lines and blue magnetic field lines form the shape of a dome. To see them better, we select some field lines and draw them in Figure 7. It can be seen from Figure 7 that the magnetic field line linkage changes divergently along the QSLs, but still remains continuous. Where the two QSL domes intersect, there is no null line, as speculated by Wang et al. (2014); there is not even a null point in this intersecting QSL structure. Some studies attribute the lack of null point in QSL domes to insufficient precision when measuring a weak magnetic field whose strength is comparable to the sensitivity of the instrument (e.g., Dalmasse et al. 2015). In addition to this reason, the dome structure here is not formed by a bunch of magnetic field lines diverging at the null point, but rather by the continuous change of the magnetic field lines along the QSLs, which does not require the presence of the null point.

For the purpose of identifying the large-scale structure of QSL domes and the HFT structure, the Q map constructed from the potential field is good enough. However, in order to identify an MFR structure, a nonpotential feature, we need to calculate the Q map using the NLFF field model. Figure 8 shows the

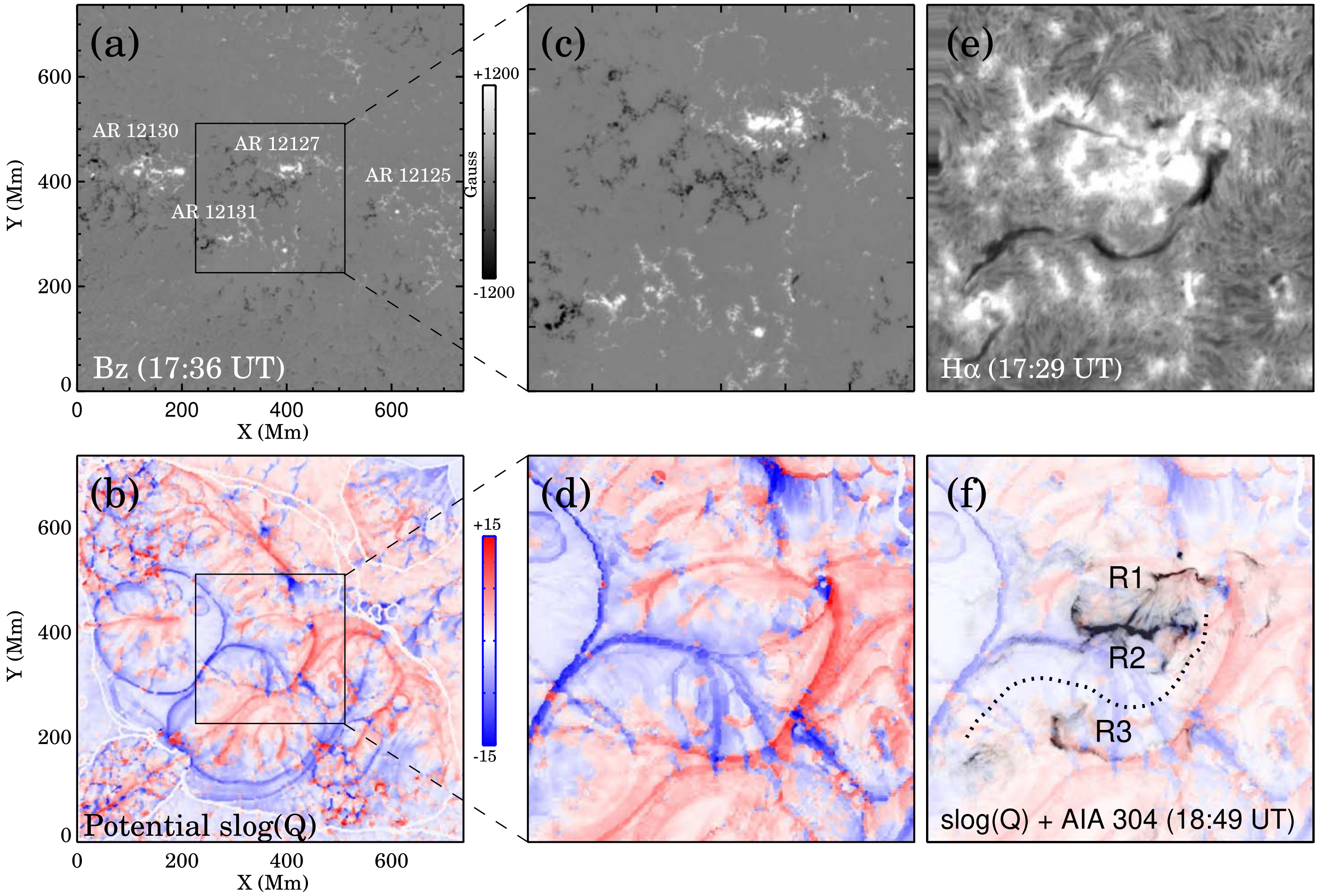

Figure 4. Magnetic field of the host AR 12127 and surrounding ARs. (a) Magnetic field B_z on which the potential field extrapolation was performed. To generate this bottom boundary for extrapolation, the HMI line-of-sight magnetogram obtained at 17:36 UT (approximately 20 minutes prior to the flare) was remapped with the CEA projection. (b) The signed logarithm of Q map (slog$Q$) at $z = 0$ km, calculated from the potential field model. The slog$Q$ map is scaled between −15 and +15, with negative values (blue) representing negative magnetic polarity and positive values (red) representing positive magnetic polarity. The boxes in the middle of (a) and (b) have the same field of view (FOV) as in Figures. 1(a), 2(a), and 3(a), and are shown enlarged in panels (c) and (d), respectively. (c)–(d) Enlarged views of the B_z and slog$Q$ maps enclosed by the boxes in (a) and (b). (e) The preflare GST Hα image, showing the filament nearby, which is well preserved during the flare. (f) The slog$Q$ map (red and blue) blended with the opposite AIA 304 Å image (gray scale). The dotted line shows the location of the filament.

slog$Q$ map derived from the NLFF field model. The NLFF field is extrapolated using the weighted optimization method (Wiegelmann 2004), from the aforementioned CEA magnetograms that are preprocessed toward the force-free field condition (Wiegelmann et al. 2006). Although the slog$Q$ maps of the NLFF field shown in Figures 8(a) and (b) are much more complex and locally different compared to that of the potential field shown in Figures 4(b) and (d), we can still barely recognize the roughly circular high-Q lines encircling AR 12130 and AR 12131. However, the portion of the high-Q line around AR 12127 inside the boxed region in Figure 8(b) is severely distorted compared with that of the potential field, implying the presence of the nonpotential fields in this region.

For a solid confirmation, we compute the twist number distribution ($T_w = \frac{1}{4\pi}\int_L \alpha dl$; Berger & Prior 2006) in that region using the code developed by Liu et al. (2016b). The resulting photospheric T_w map (Figure 8(c)) shows two regions with enhanced T_w in the negative sign, which could be conjugate footpoints of a twisted bundle of magnetic field lines, known as an MFR. This result suggests that an MFR should exist between the two separating ribbons R1 and R2, although we do not see it in the Hα line images. The MFR is approximately 30 Mm high, which is among the highest MFRs ever found in the comprehensive study of the NLFF field model (e.g., Jing et al. 2018). The height of the MFR is larger than the typical height of the Hα line formation, which explains why we could not see it in the Hα observations. The height predicted by the model is also consistent with the observation that R1 and R2 are far apart from each other, ∼15 Mm, from the beginning of the flare (see Figure 2(b)). If the MFR were low-lying, R1 and R2 could not have developed beneath it. The MFR is highly twisted, with $|T_w|$ mostly in the range of 1.8–2.4. Figures 8(d) and (e) show more explicitly the MFR structure as derived from the NLFF field model. On the other hand, in the observed Hα filament region between R2 and R3, $|T_w|$ is essentially smaller than 0.3. From this point of view, the MFR between R1 and R2 has a greater potential for eruption than the filament between R2 and R3.

2.3. The Confined Filament

In MHD simulations, it is common to consider both kink instability (measured by twist) and torus instability (measured by decay index) when investigating the cause of eruptions. In particular, the gradient of the magnetic field above an MFR

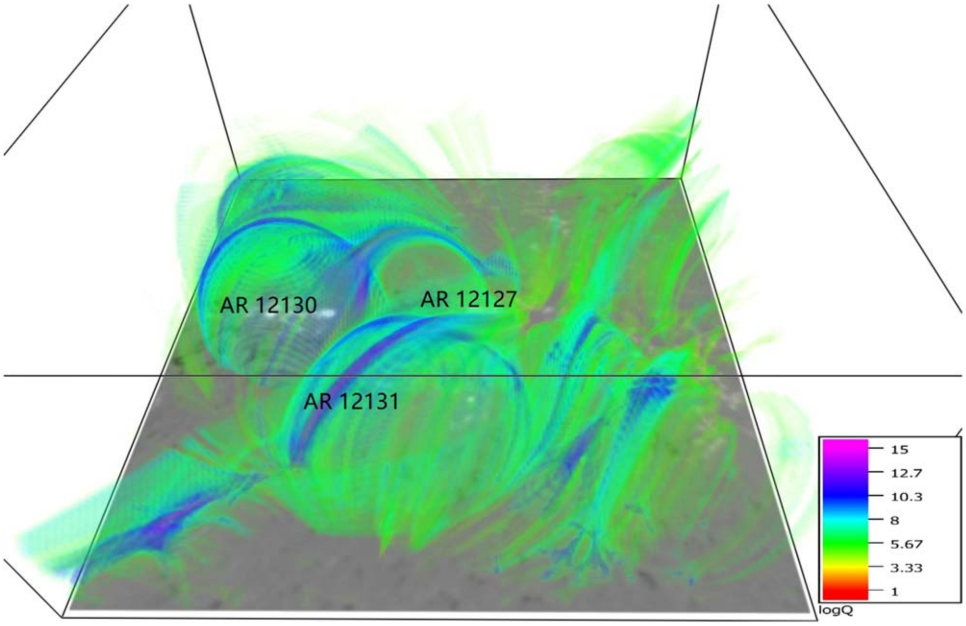

Figure 5. 3D distribution of the unsigned logarithm of the Q factor (log$Q$) in the height range from 0 to 150 Mm, superimposed on the photospheric magnetic field B_z. To better visualize the QSL dome structure, the QSLs are rendered as semitransparent surfaces scaled according to log$Q$, and we screen out the Q factors with logarithms lower than 4. The base B_z map has the same FOV as that of Figure 4(a).

with height h, known as decay index, $n = -\partial \log B_{\rm ex}/\partial \log h$, is thought to be the main determinant of whether the MFR will eventually evolve into a CME. A steep gradient indicates a rapid decay of the overlying magnetic field with increasing height. When the decay index exceeds a critical value, typically $n \geqslant n_{\rm crit} = 1.5$, torus instability comes into play and the MFR develops into a CME. We compute the decay index n over the FOV of the potential field and the result is shown in Figure 9(a), where the value of each point represents n derived from a linear fit to the potential field strength $\log B_{\rm ex}$ and height $\log h$ over the height range from 40 Mm to 105 Mm. This height range was originally proposed by Liu (2008) because CME activation typically occurs in this height range, and is adopted by many subsequent studies (e.g., Xu et al. 2012; Jing et al. 2015). Figure 9(b) shows two examples of using linear fits to calculate n, one decaying quickly and the other decaying slowly. Figures 9(c) and (d) are enlarged views of the n map in the flare region, including the magnetic field as well as the positions of the Hα filament and flare. It is clear that the R1/R2 pair (and the twisted MFR in between) occurs in the region where the magnetic field decays rapidly with height ($n \sim 1.5$), where the MFR is more vulnerable to torus instability. On the other hand, the Hα filament resides in the region of relatively slow decay of magnetic field ($n < 1$), which helps to confine the filament in place. This may explain, from the point of view of torus instability, why the eruption occurred between R1 and R2 and the filament did not erupt with the flare.

2.4. Photospheric Flows

We also study the photospheric surface flows to help understand the magnetic field of the AR prior to the flare. We use the following two methods and data to derive surface flow velocities: (1) the local correlation tracking (LCT) method for the time sequence of continuum images; (2) the substantially improved version of the differential affine velocity estimator (DAVE4VM; Schuck 2008) for the time sequence of vector magnetograms. The LCT method tracks features by locating the maximum cross-correlation of windowed features between two images (Fisher & Welsch 2008), and DAVE4VM uses the induction equation to derive flow fields (Schuck 2008). Both continuum images and vector magnetograms are provided by SDO/HMI SHARP CEA data series, from 10 UT (∼8 hr before the flare onset) to 18:48 UT (the end of the flare), with a cadence of 12 minutes and pixel size of 0.″5.

As shown in Figure 10(a), the position of the AR 12127 sunspot cluster is highly coincident with the footpoints of one of the QSL domes. The region of apparent surface flow motion is concentrated only on this sunspot cluster, as marked by the box in Figure 10(a). Figures 10(b) and (c) show the flow maps averaged over the above period obtained by the LCT and DAVE4VM methods, respectively. Although the results shown in the two panels are not quite consistent, we notice that both maps show relatively strong surface flow in the area near (47 Mm, 37 Mm) in (b) and (c), with velocities up to 0.1 ± 0.05 km s^{-1} in continuum flows and 0.3 ± 0.1 km s^{-1} in magnetic flows. This small region of flows is adjacent to the westernmost sunspots of AR 12127, and the flow motion causes the sunspots to rotate clockwise to some extent. Figure 10(d) shows the initial brightening of the flare as observed with high-resolution GST 10830 Å data. This region is where the flare initially brightens.

Due to the line-tying effect, it is generally believed that the forced motion of the photospheric footpoints of coronal magnetic field lines is the primary source for the helicity and energy buildup in the corona and may ultimately drive the coronal magnetic field out of equilibrium or into instability. We calculate the free magnetic energy stored in the corona using $E_{\rm free} = \int \boldsymbol{B}_{\rm NLFF}^2 dV - \int \boldsymbol{B}_{\rm p}^2 dV$, where $\boldsymbol{B}_{\rm NLFF}$ and $\boldsymbol{B}_{\rm p}$ are NLFF field and potential field, which are extrapolated using the aforementioned weighted optimization method (Wiegelmann 2004) and a Green's function method (Aly 1989), respectively. The boundary conditions used for extrapolations are also from the 12-minute cadence HMI SHARP CEA vector magnetogram

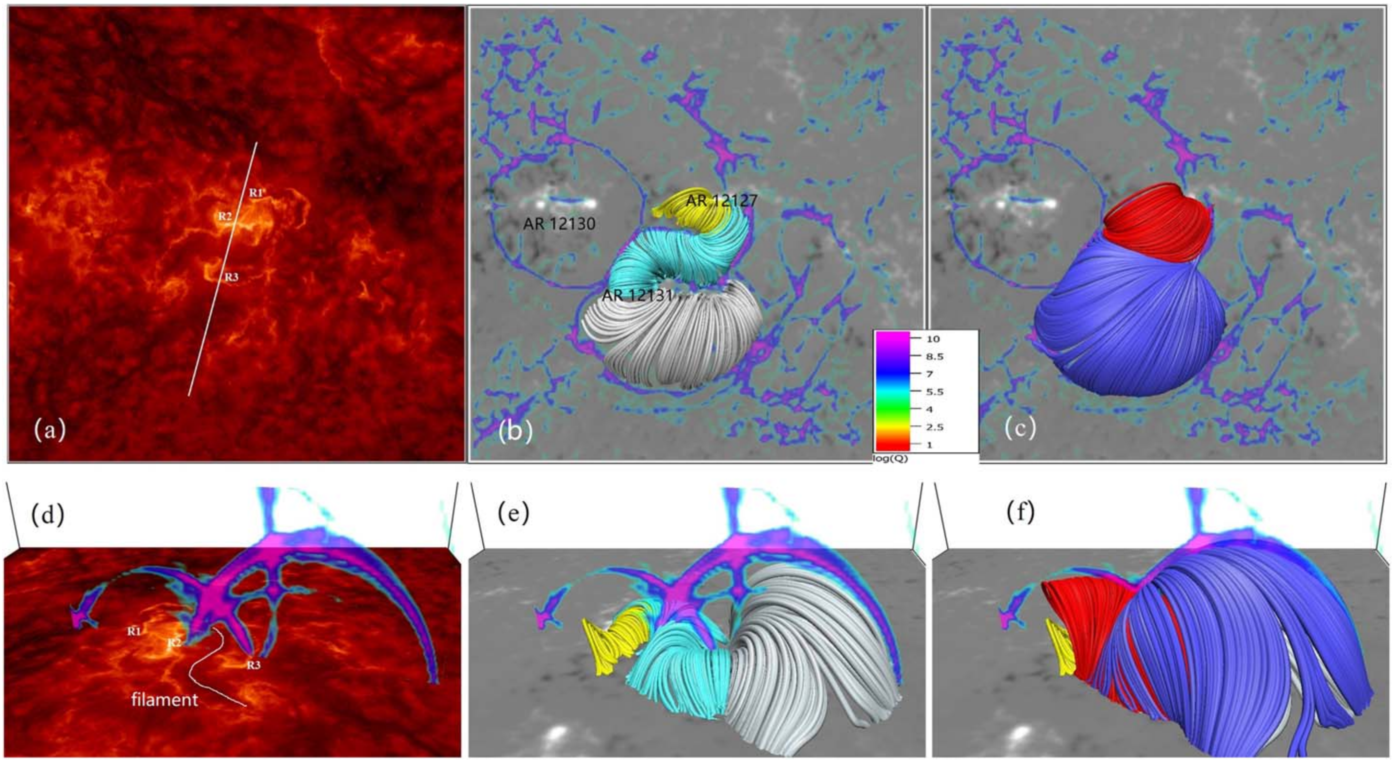

Figure 6. 3D Magnetic configuration. (a) AIA 304 Å image, same FOV as in Figures 4(a) and 5, and remapped with CEA projection. The solid line indicates the location of the vertical cut shown in (d). (b) Magnetic field lines below the QSL domes, superimposed on the magnetic field B_z. The magnetic field lines are grouped by color according to their connectivity domains. The log$Q$ map is also plotted over B_z. (c) Same as (b), but the magnetic field lines are about the same height as the QSL domes. (d) The vertical cross-section slice of log$Q$ through the virtual slit in (a), viewed from the east. (e), (f) Side views of the magnetic field lines shown in (b) and (c) from the east, respectively. The figure is accompanied by an animation. The left side of the animation shows a mixed B_z and log$Q$ structure in the x–y plane with a moving slit superimposed on it. The right side of the animation shows the vertical cross section of the log$Q$ structure corresponding to the position of the slit. The duration of the animation is 2 s.

data, but over a time period from 14 UT to 19:48 UT and rebinned to 1″ pixel scale. The FOV we used for the extrapolations is the same as the FOV of Figure 4(c). The computational domain for extrapolations is $400 \times 400 \times 200$ uniform grid points (corresponding to $\sim 290 \times 290 \times 145$ Mm^3). With the same series of NLFF and potential field models, we also calculate the relative magnetic helicity (Berger & Field 1984) of AR 12127 in the form used by Finn & Antonsen (1985), $H_r = \int_V (\boldsymbol{A} + \boldsymbol{A}_p) \cdot (\boldsymbol{B}_{\rm NLFF} - \boldsymbol{B}_{\rm p}) dV$, where $\boldsymbol{A}$ and $\boldsymbol{A}_p$ are vector potentials of $\boldsymbol{B}_{\rm NLFF}$ and $\boldsymbol{B}_{\rm p}$, respectively. We adopt the code of Fan (2009) to determine the two vector potentials from the extrapolated NLFF and potential field models. To calculate the total electric current, we set up a vertical cross section across the MFR and the rotational flows. The black line in Figure 10(a) shows the intersection of this vertical cross section with the surface.

Figure 10(e) shows the temporal evolution of total electric current $|\boldsymbol{I}|$, free magnetic energy $E_{\rm free}$ and relative magnetic helicity H_r, where $|\boldsymbol{I}|$ is computed by integrating horizontal current density $|\boldsymbol{j}_h|$ passing through the vertical cross-sectional area, and the latter two calculated over the entire extrapolation domain. As shown in Figure 10(e), electric current and magnetic helicity (in negative sign) continue to accumulate before the flare, and decrease after the flare. The accumulation of free magnetic energy is not as pronounced as that of the other two, but the energy decrease after the flare is. It is noteworthy that the reduction in electric current and helicity and energy release start at about 30 minutes before the flare (the blue-filled section), suggesting that the relaxation of the coronal magnetic field occurs before the flare-associated magnetic reconnection takes place. Such magnetic field relaxation is also implied by the slow expansion of coronal loops connecting R1 and R2 before the flare.

The bottom panels of Figure 10 show the spatial distribution of the horizontal current density $|j_h|$ in the vertical section, from before the flare to the end of the flare. Obvious current changes are manifested in the MFR: the current density within the MFR structure increases before the flare (Figures 10(f), (g)) and shows a tendency to extend upward as the flare occurs (Figure 10(h)), and this structure weakens in the later stage of the flare (Figure 10(i)). However, we could not find, in the models, a consistent pattern of a strong current buildup associated with the flare. This is not surprising because the NLFF field model and other extrapolation models are based on the assumption that the coronal magnetic field is always in static equilibrium, and therefore are not suitable for reproducing the rapidly evolving magnetic field and dynamics during the eruption (Jiang et al. 2022).

3. Discussion

We discuss the 3D magnetic structure implied by the three flare ribbons, the role of sunspot rotation in causing the eruptive flare, and the confined filament as major characteristics of this flare event.

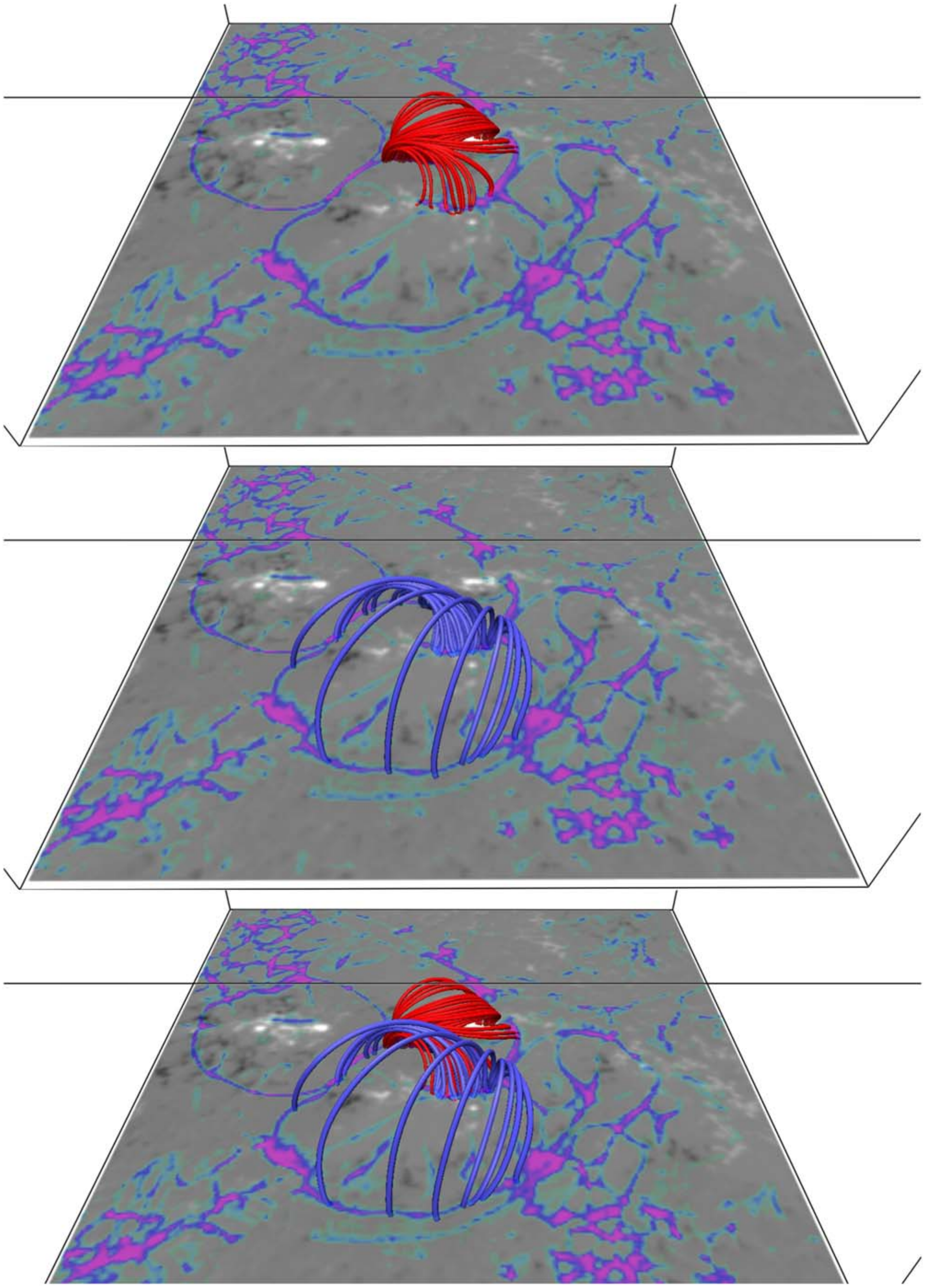

Figure 7. Magnetic field lines on the two intersecting QSLs, superimposed on the magnetic field B_z. The log$Q$ map is also plotted over B_z. The FOV is the same as Figure 4(a).

3.1. Three Flare Ribbons

Wang et al. (2014) proposed that three-ribbon flares occur in a fishbone-like magnetic structure with a null line embedded in the middle. We further the discussion of the 3D magnetic structure with the observation and analysis of the lager-scale three-ribbon flare studied here. Of the three ribbons, R1 and R2 behave like a pair of separating ribbons as in a typical two-ribbon flare, while R3 appears slightly later and remains stationary. The key magnetic structure consists of two QSL domes intersecting to form an HFT. The three flare ribbons are well accommodated and linked by this topological structure: R1/R2 are located on one of the three sub-arcs under the QSL domes, and R3 is spatially coincident with the footpoints of one of the QSL domes. Although we fail to find an erupting filament between R1 and R2 in the observed images, we could infer the presence of such a filament-like MFR located there from the NLFF field model, and also from the observed separating motions of R1 and R2. In this case, the MFR erupting above R1 and R2 is consistent with the standard flare reconnection model, which, in combination with the QSL reconnection (slipping or slip-running), can well explain the observed three flare ribbons.

A simplified version of the magnetic structure involved in this flare is shown schematically in Figure 11. The magnetic structure of this three-ribbon flare is very similar in nature to the one proposed by Wang et al. (2014), with the only

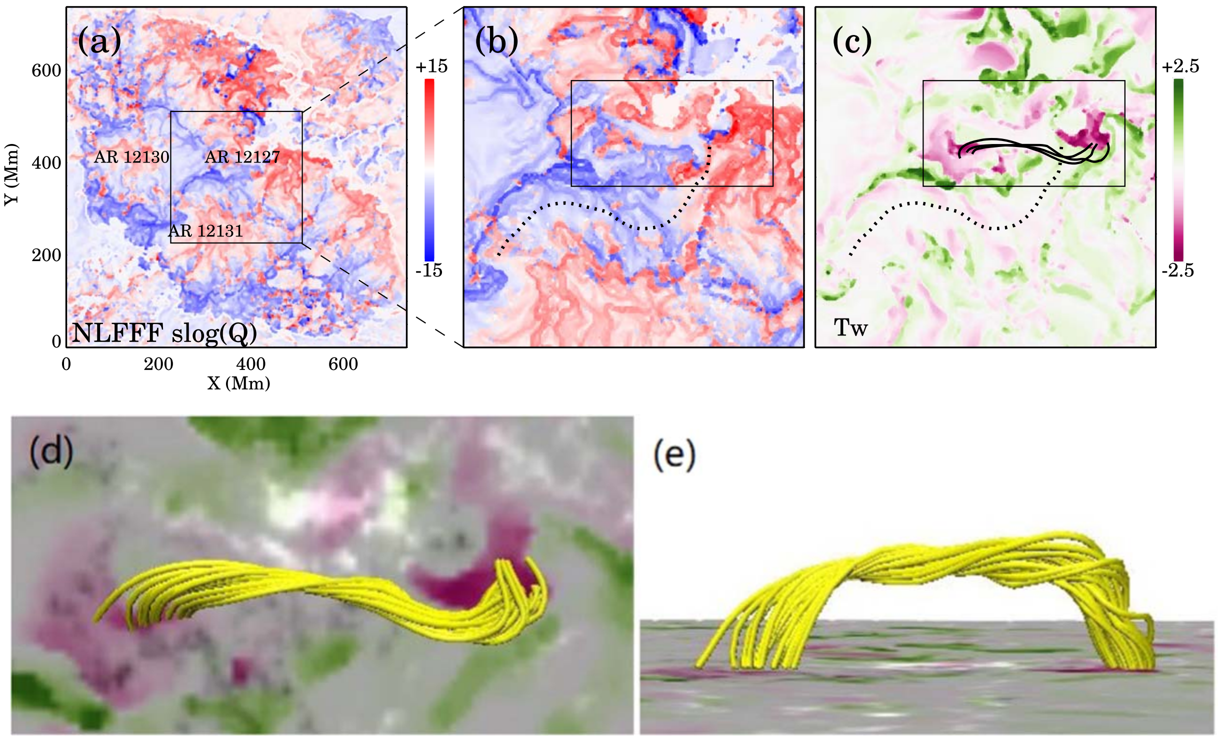

Figure 8. (a), (b) slog$Q$ maps computed from the NLFF field, with the same FOV as in Figure 4(b) and 4(d), respectively, but at $z \sim 2100$ km to make NLFF slog$Q$ maps less complex. (c) Photospheric T_w map computed from the NLFF field, with the same FOV as in (b), with a few magnetic field lines (black) superimposed on it. The dotted line shows the location of the filament. The rectangles in (b) and (c) mark the FOV of (d) for close-up viewing. (d) T_w map blended with magnetic field B_z map, with an MFR superimposed on it. The two footpoints of the MFR are located at the conjugate regions of enhanced T_w. (e) 3D perspective of the MFR.

difference being that the fishbone structure that hosts the three-ribbon flare is no longer a 2.5D symmetric structure involving a null line, but rather a true 3D configuration involving a pronounced HFT that runs essentially in the direction of the ribbons. For flares with three parallel ribbons, although they each have their own characteristics and their specific magnetic structures may be different, the fishbone structure as the magnetic skeleton is what they have in common. We believe that the HFT structure can better adapt to the fishbone structure of three-ribbon flares in a broad sense, with or without null points, on both small and large scales. In such a topology, perturbations in any part of the structure may trigger magnetic reconnection in other parts (Parnell et al. 2008; Dalmasse et al. 2015).

3.2. Role of Surface Flows

Our LCT and DAVE4VM analysis shows the rotational surface flow motions near the sunspots that coincide with the initial flare brightening. When the flare occurred, R1 and R2 formed at one arcade domain of the HFT, and R3 is activated a little later than R1 and R2 at another arcade domain.

If the photospheric rotational flows substantially weaken the downward magnetic tension of an MFR, as shown in some MHD simulations (e.g., Török et al. 2013; Jing et al. 2021), the MFR can no longer maintain an equilibrium between the upward hoop force and downward strapping force and tension force, and thus expands upward. The torus instability sets in when the MFR expands to a point where the decay index of the strapping field exceeds the critical value. The “flare reconnection” then takes over, accelerating the expulsion as a CME. Since the primary flare R1/R2 occurs within one of the two linked QSLs, the eruption between R1 and R2 is likely to stress the magnetic field of the QSLs and transmit the magnetic stress along the QSLs, eventually triggering a QSL reconnection, leading to the occurrence of R3.

Although the eruption between R1 and R2 may have triggered another instance of QSL reconnection in the HFT between R2 and R3, it is yet unknown whether the QSL reconnection at the HFT should also trigger an eruption of the filament located below the HFT. The rotation of the sunspots may enhance the strapping fields over the filament by adding more twist to the QSL, to prevent the filament eruption. This can explain why any eruption signatures in this event are weak overall, except for the rising flare loop between R1 and R2 at the time of flare onset. This event presents a case that a successful eruption of a filament inside a circular separatrix dome is not a must for all types of circular ribbon flares.

It is also possible that the photospheric rotational flow may have resulted in the “magnetic pinching,” which can lead to the fast formation of a current layer in HFTs. In Titov et al. (2003) model, the magnetic pinching is caused by the large-scale shearing motions that are applied to the footpoints of the HFT. As a result, the unbalanced magnetic stress accumulates in the middle of the HFT, eventually leading to an exponentially fast pinching of the HFT into a thin current layer to produce the flare. The rotational flow we observed may have asymmetrically distorted the HFT, leading to the magnetic pinching and subsequent eruption. In addition, the magnetic pinching may lead to the formation of a nearly vertically oriented current layer, as shown in Figure 11(c). The magnetic reconnection in this layer should feed up the flux in the mid-arcade containing the visible filament, making it more difficult to erupt due to the enhanced strapping effect. We are, however, unable to identify the corresponding current layer evolution or increasing

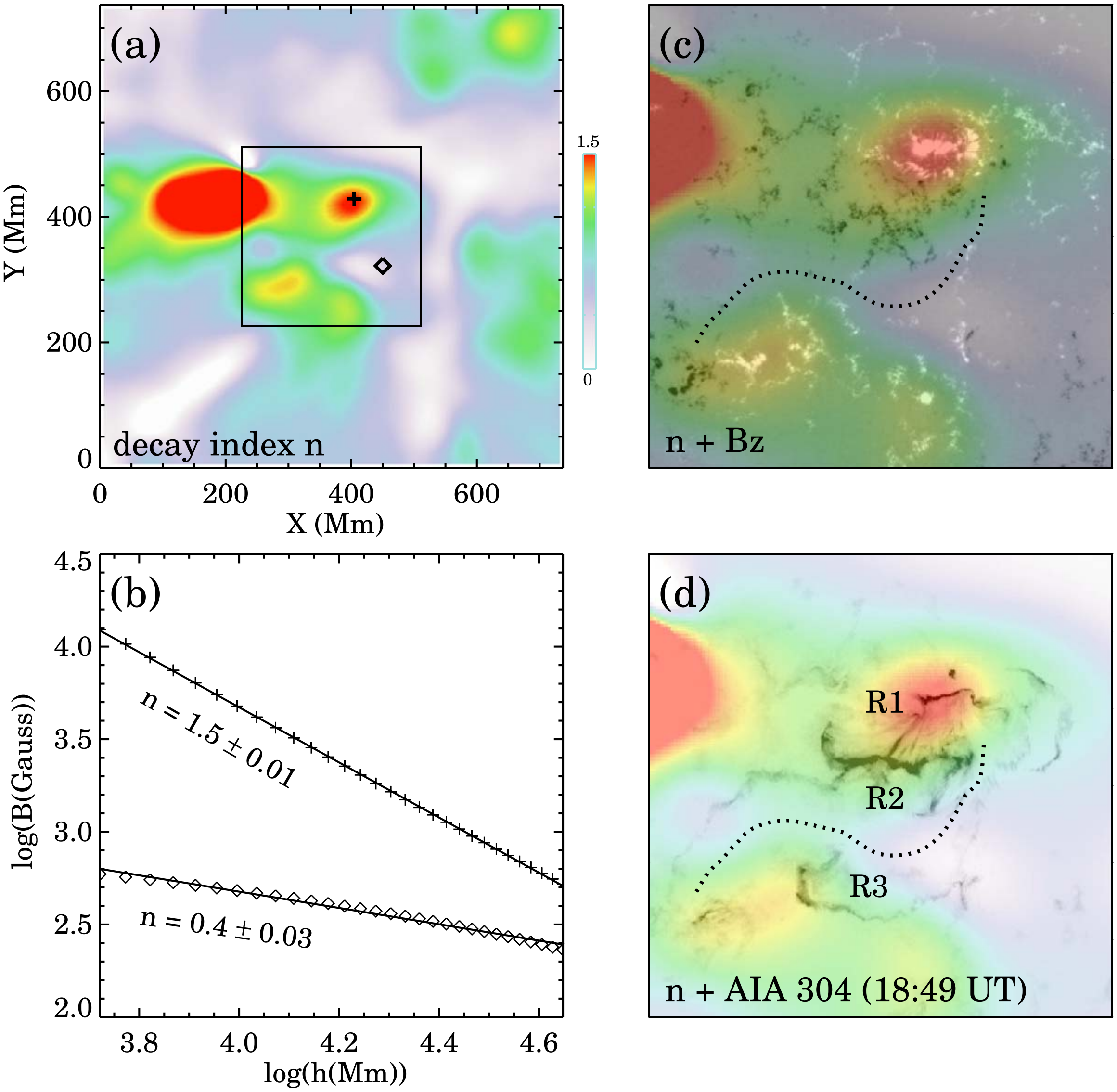

Figure 9. Decay index of the magnetic field. (a) The map of decay index, calculated by fitting potential magnetic field strength over the 40–100 Mm height range. The FOV is the same as in Figures 3(a), 4, 5, and 6. The box in the middle marks the area for zoomed-in view in (c) and (d). The positions of the two fitting examples are marked with plus and diamond symbols. (b) Two examples of fitting magnetic field and height. Both strength and height are in log units. The solid lines show the results of the linear fit to the data, and the slope is the decay index as detailed in Liu (2008). (c) Zoomed-in decay index map (color), blended with B_z (black and white). (d) Zoomed-in decay index map (color), blended with the opposite AIA 304 Å image (black and white). The dotted curve delineates the position of the filament.

magnetic pinching in our NLFF field models, probably because the NLFF field extrapolation models are incapable of producing such a dynamic buildup of current layer. We anticipate that recently developed data-driven MHD simulations would help model the possible role of the photospheric flow motions in the magnetic pinching of the HFT.

3.3. The Confined Filament

It is of general interest in the discussion of the breakout eruption whether or not a filament inside a circular separatrix dome successfully erupts. If not, it is called a failed eruption. In the present event, the filament under the HFT is almost intact, with only a small strand of material erupting with the flare. Such cases of successful eruption overall, despite the failed eruption of filaments, have previously been reported by Liu et al. (2014) and Chintzoglou et al. (2017). In both cases, the HFT topology played a key role in holding a filament from eruption, but each case showed distinct characteristics too.

Chintzoglou et al. (2017) presented a case in which the filament is located at the supra-arcade flux domain, i.e., the large-scale connectivity of the two exterior polarities of the intersecting QSLs. The expansion of the filament pushes the supra-arcade, and the reconnection at the HFT shreds out the rising filament. Liu et al. (2014) named their event an unorthodox long-duration confined flare in which an HFT has two neighboring sheared arcades, and one of them harbors a filament. That filament survives the flare owing to the strong confining field of the sheared arcade. The present event is not the same as that of Chintzoglou et al. (2017) because the filament is located below the arcades. It is similar to that of Liu et al. (2014) in that eruption is successful in one arcade and the filament stays intact in the other arcade. As a difference, we point out the sunspot rotation as the cause of the eruptive flare

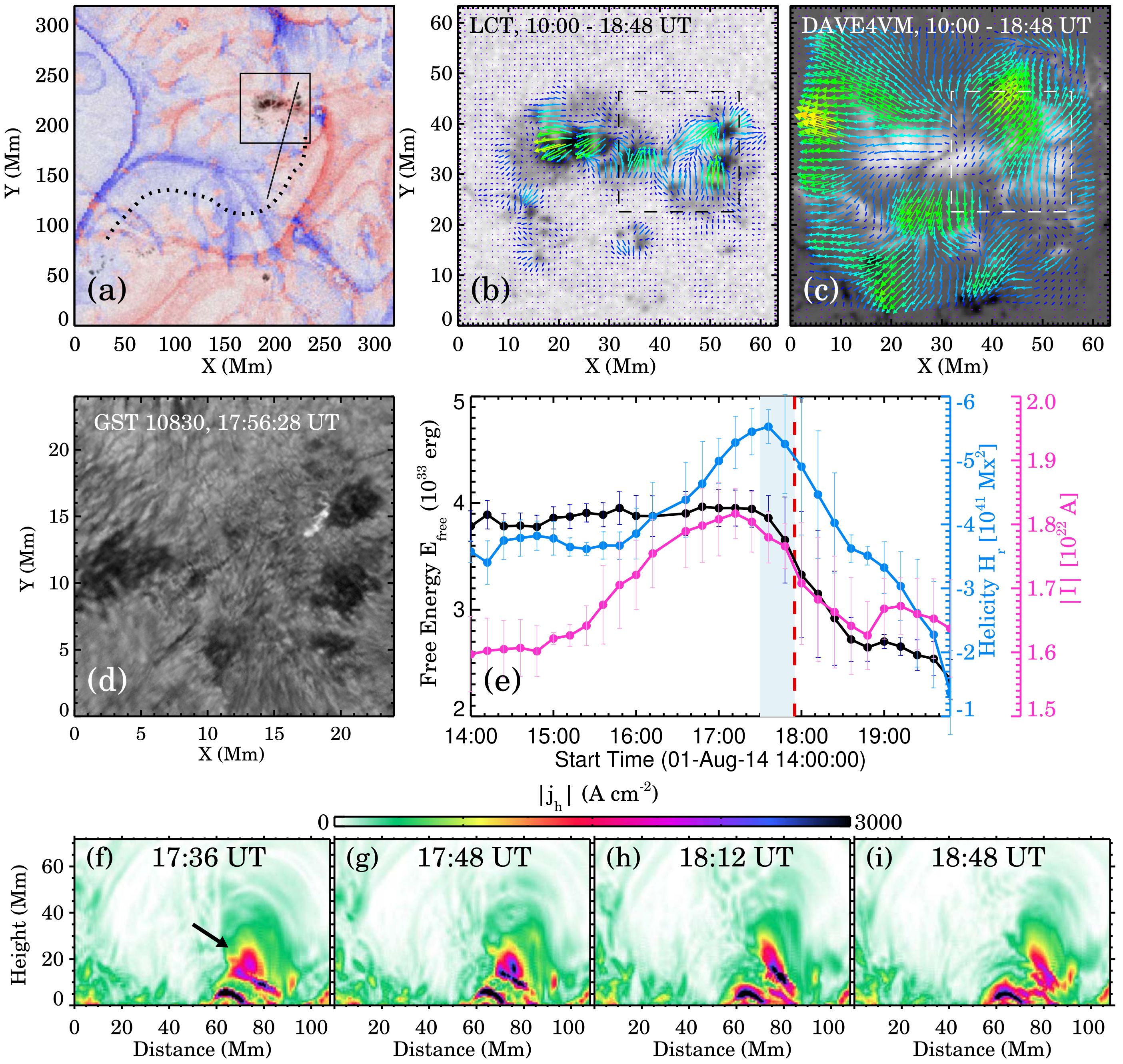

Figure 10. (a) Same as Figure 4(d) but blended with an HMI continuum image to show the location of the sunspot cluster in the QSL system. The black line indicates where the vertical cross section of current density (see bottom panels) intersects the surface, and the box marks the FOV of (b) and (c). (b) HMI continuum image, with superimposed arrows showing flows calculated with the LCT method. (c) HMI magnetogram B_z, with superimposed arrows showing flows obtained with the DAVE4VM method. The flows are averaged between 10:00 UT and 18:48 UT. The dashed boxes mark the FOV of (d). (d) BBSO GST 10830 Å image, at the very beginning of the flare. (e) Temporal variation of free magnetic energy $E_{\rm free}$ (black), relative magnetic helicity H_r (blue), and total current $|I|$ (pink). The error bars show the running standard deviation for five consecutive data points. The red vertical dashed line marks the start time of the flare, and the shaded area marks the period of time during which the slow rise of the coronal loop was observed prior to the flare. (f)–(i) Distributions of horizontal current density $|j_h|$ on the vertical cross section (viewed from the right) at four times. The arrow indicates the MFR structure between R1 and R2.

above R1-R2, whereas a newly emerging magnetic flux triggers the flare in the event of Liu et al. (2014).

The rather stationary R3 dictates a continuous exchange of connectivity between neighboring magnetic lines through a QSL reconnection, which does not destroy the magnetic structure, and as a result, the filament could remain confined. This is similar to the Type I confined flares proposed by Li et al. (2019). The strong confinement of the filament by the overlying magnetic field is manifested by a decay index being below the critical value for torus instability. Furthermore, as mentioned before, in the HFT configuration shown in Figure 11(b), any perturbations caused by both the erupting invisible filament and the rotational motion across the QSL footpoints can lead to an HFT pinching as well as the formation of the current layer that is oriented almost vertically (see Figure 11(c)). Reconnection in this layer should feed up the flux in the mid-arcade that contains the filament by increasing its strapping power.

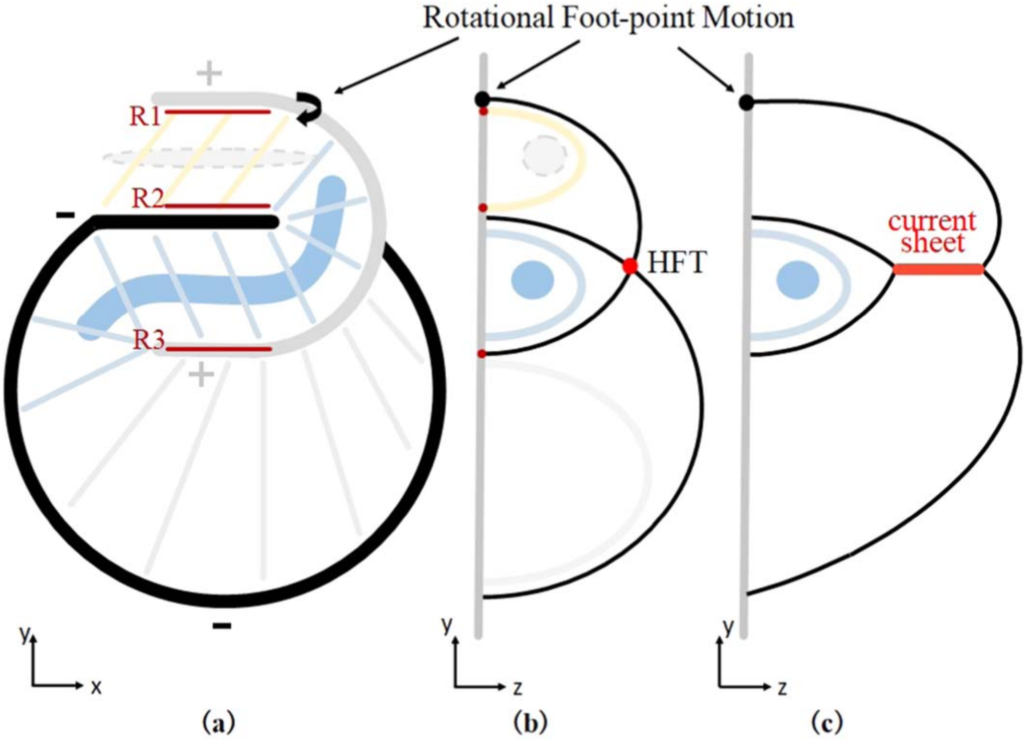

Figure 11. Schematic representation of the magnetic configuration. In (a), the QSL footprints (high-Q lines) located in the positive and negative magnetic fields are represented by thick gray and black lines, respectively, while the thin lines represent the magnetic field lines under the QSL domes grouped by color according to location (same as in Figure 6(b)). Flare ribbons R1 and R2 are located between two positive and negative high-Q lines and are connected by light yellow magnetic lines, while the position of R3 coincides with the footpoints of a QSL. The gray bar between R1 and R2 and the blue bar between R2 and R3 represent the invisible MFR and the observed confined filament, respectively. In (b), the black line outlines two intersecting QSLs, forming the HFT. In (c), a vertical current sheet forms due to the eruption and magnetic pinching associated with the rotational flow motion. The accumulation of reconnected magnetic flux in the mid-arcade further enhances the magnetic confinement of the visible filament underneath.

4. Summary and Conclusion

To summarize, we presented observations and analysis of an eruptive M1.5 flare from NOAA AR 12127, characterized by the three flare ribbons and a stationary filament as detected by the SDO/AIA, and the rotating sunspot motions as determined from a series of SDO/HMI magnetograms. We conclude that a combination of the standard two-ribbon flare reconnection and the QSL reconnection can account for the observed three ribbons and the stationary filament based on the following results.

1. The observed three flare ribbons are consistent with a magnetic topology involving two intersecting QSLs forming an HFT, which is more obvious in this larger-scale flare event.
2. Two of the three ribbons show separation consistent with the standard reconnection scenario for eruptive flares. The NLFF field extrapolation model implies the presence of an MFR between the two separating ribbons. The third ribbon is fixed alongside the filament remaining confined, for which we suggest the QSL reconnection at the HFT.
3. The surface flow motion characterized by the rotating sunspot motions may lead to the energy buildup and cause the standard eruption to occur in the two-ribbon area. The relaxation of the magnetic field starts before the flare and continues throughout the flare.
4. The filament is located in the region interlocked by two QSL domes, and the HFT reconnection may have strengthened the overlying strapping fields to prevent the filament from erupting.

The overall picture derived for this event differs from the previously known scenario for circular ribbon flares in which a successful filament eruption causes the circular ribbon flare to proceed. Our results suggest that the magnetic eruption out of circular separatrices can occur in a combination of standard reconnection and additional 3D magnetic reconnection depending on the complexity of magnetic configuration.

Acknowledgments

The authors are grateful to the anonymous referee for the valuable comments. We thank the NASA SDO team for HMI and AIA data. HMI and AIA are instruments on board SDO, a mission for NASA’s Living With a Star program. We gratefully acknowledge the use of data from the Goode Solar Telescope (GST) of the Big Bear Solar Observatory (BBSO). BBSO operation is supported by US NSF AGS-2309939 and AGS-1821294 grants and the New Jersey Institute of Technology. GST operation is partly supported by the Korea Astronomy and Space Science Institute and the Seoul National University. We thank Dr. Jiasheng Wang for his help in surface flow analysis when he was an employee of NJIT. J.J., J.L., Q.L., J.W., N.L., S.I., Y.X., and H.W. were supported by NASA grants 80NSSC23K0406 (HGI), 80NSSC21K1671 (HSR), 80NSSC21K0003 (LWS), 80NSSC19K0068, 80NSSC19K0257, 80NSSC19K0859, 80NSSC24K0258, and NSF grants AGS 1927578, 1954737, 2114201, 2149748 (ANSWERS), 2300341 (SHINE), 2309939, 2145253, 2228996, and 2204384. M.M. is supported by the DKIST Ambassador Program, funding for which is provided by the National Solar Observatory, a facility of the National

Science Foundation, operated under Cooperative Support Agreement number AST-1400450.

ORCID iDs

Ju Jing https://orcid.org/0000-0002-8179-3625
Jeongwoo Lee https://orcid.org/0000-0002-5865-7924
Qin Li https://orcid.org/0000-0002-3669-1830
Nian Liu https://orcid.org/0000-0002-6018-3799
Satoshi Inoue https://orcid.org/0000-0001-5121-5122
Haimin Wang https://orcid.org/0000-0002-5233-565X

References

Aly, J. J. 1989, SoPh, 120, 19
Arnold, H., Drake, J. F., Swisdak, M., et al. 2021, PhRvL, 126, 135101
Aulanier, G., Pariat, E., Démoulin, P., & Devore, C. R. 2006, SoPh, 238, 347
Aulanier, G., Pariat, E., & Démoulin, P. 2005, A&A, 444, 961
Bamba, Y., Inoue, S., Kusano, K., & Shiota, D. 2017, ApJ, 838, 134
Berger, M. A., & Field, G. B. 1984, JFM, 147, 133
Berger, M. A., & Prior, C. 2006, JPhA, 39, 8321
Cannon, B., Jing, J., Li, Q., et al. 2023, ApJ, 950, 144
Carmichael, H. 1964, NASSP, 50, 451
Chintzoglou, G., Vourlidas, A., Savcheva, A., et al. 2017, ApJ, 843, 93
Craig, I. J. D., & Effenberger, F. 2014, ApJ, 795, 129
Dahlin, J. T., Antiochos, S. K., Qiu, J., & DeVore, C. R. 2022, ApJ, 932, 94
Dalmasse, K., Chandra, R., Schmieder, B., & Aulanier, G. 2015, A&A, 574, A37
Demoulin, P., Bagala, L. G., Mandrini, C. H., Henoux, J. C., & Rovira, M. G. 1997, A&A, 325, 305
Effenberger, F., Thust, K., Arnold, L., Grauer, R., & Dreher, J. 2011, PhPl, 18, 032902
Fan, Y. 2009, ApJ, 697, 1529
Finn, J. M., & Antonsen, T. M. J. 1985, CoPPC, 9, 111
Fisher, G. H., & Welsch, B. T. 2008, in ASP Conf. Ser. 383, Subsurface and Atmospheric Influences on Solar Activity, ed. R. Howe et al. (San Francisco, CA: ASP), 373
Fletcher, L., & Hudson, H. 2001, SoPh, 204, 69
Forbes, T. G., & Priest, E. R. 1984, SoPh, 94, 315
Goode, P. R., & Cao, W. 2012, in ASP Conf. Ser. 463, Second ATST-EAST Meeting: Magnetic Fields from the Photosphere to the Corona., ed. T. R. Rimmele et al. (San Francisco, CA: ASP), 357
Hirayama, T. 1974, SoPh, 34, 323
Jiang, C., Feng, X., Guo, Y., & Hu, Q. 2022, Innov, 3, 100236
Jing, J., Inoue, S., Lee, J., et al. 2021, ApJ, 922, 108
Jing, J., Liu, C., Lee, J., et al. 2018, ApJ, 864, 138
Jing, J., Qiu, J., Lin, J., et al. 2005, ApJ, 620, 1085
Jing, J., Xu, Y., Lee, J., et al. 2015, RAA, 15, 1537
Joshi, N. C., Joshi, B., & Mitra, P. K. 2021, MNRAS, 501, 4703
Joshi, N. C., Sterling, A. C., Moore, R. L., Magara, T., & Moon, Y.-J. 2017, ApJ, 845, 26
Kazachenko, M. D., Lynch, B. J., Welsch, B. T., & Sun, X. 2017, ApJ, 845, 49
Kopp, R. A., & Pneuman, G. W. 1976, SoPh, 50, 85
Lee, J. 2022, RvMPP, 6, 32
Lee, J., & Gary, D. E. 2008, ApJ, 685L, 87
Lee, J., Karpen, J. T., Liu, C., & Wang, H. 2020, ApJ, 893, 158
Lemen, J. R., Title, A. M., Akin, D. J., et al. 2012, SoPh, 275, 17
Li, T., Liu, L., Hou, Y., & Zhang, J. 2019, ApJ, 881, 151
Li, Y., Qiu, J., Longcope, D. W., Ding, M. D., & Yang, K. 2016, ApJL, 823, L13
Liu, C., Prasad, A., Lee, J., & Wang, H. 2020, ApJ, 899, 34
Liu, R., Chen, J., Wang, Y., & Liu, K. 2016a, NatSR, 6, 34021
Liu, R., Kliem, B., Titov, V. S., et al. 2016b, ApJ, 818, 148
Liu, R., Titov, V. S., Gou, T., et al. 2014, ApJ, 790, 8
Liu, Y. 2008, ApJL, 679, L151
Longcope, D. W. 2005, LRSP, 2, 7
Mandrini, C. H., Schmieder, B., Démoulin, P., Guo, Y., & Cristiani, G. D. 2014, SoPh, 289, 2041
Masson, S., Pariat, E., Aulanier, G., & Schrijver, C. J. 2009, ApJ, 700, 559
Masson, S., Pariat, É., Valori, G., et al. 2017, A&A, 604, A76
Mitra, P. K., Veronig, A. M., & Joshi, B. 2023, A&A, 674, A154
Naus, S. J., Qiu, J., DeVore, C. R., et al. 2022, ApJ, 926, 218
Neupert, W. M. 1968, ApJL, 153, L59
Parnell, C. E., Haynes, A. L., & Galsgaard, K. 2008, ApJ, 675, 1656
Pesnell, W. D., Thompson, B. J., & Chamberlin, P. C. 2012, SoPh, 275, 3
Priest, E. R., & Démoulin, P. 1995, JGR, 100, 23443
Qiu, J., Hu, Q., Howard, T. A., & Yurchyshyn, V. B. 2007, ApJ, 659, 758
Qiu, J., Lee, J., Gary, D. E., & Wang, H. 2002, ApJ, 565, 1335
Qiu, J., Wang, H., Cheng, C. Z., & Gary, D. E. 2004, ApJ, 604, 900
Qiu, Y., Guo, Y., Ding, M., & Zhong, Z. 2020, ApJ, 901, 13
Reid, H. A. S., Vilmer, N., Aulanier, G., & Pariat, E. 2012, A&A, 547, A52
Saba, J. L. R., Gaeng, T., & Tarbell, T. D. 2006, ApJ, 641, 1197
Sahu, S., Joshi, B., Mitra, P. K., Veronig, A. M., & Yurchyshyn, V. 2020, ApJ, 897, 157
Schou, J., Scherrer, P. H., Bush, R. I., et al. 2012, SoPh, 275, 229
Schuck, P. W. 2008, ApJ, 683, 1134
Sturrock, P. A. 1966, Natur, 211, 695
Sun, X., Hoeksema, J. T., Liu, Y., et al. 2013, ApJ, 778, 139
Titov, V. S., Galsgaard, K., & Neukirch, T. 2003, ApJ, 582, 1172
Titov, V. S., Hornig, G., & Démoulin, P. 2002, JGRA, 107, 1164
Titov, V. S., Mikić, Z., Linker, J. A., Lionello, R., & Antiochos, S. K. 2011, ApJ, 731, 111
Török, T., Temmer, M., Valori, G., et al. 2013, SoPh, 286, 453
Wang, H., & Liu, C. 2012, ApJ, 760, 101
Wang, H., Liu, C., Deng, N., et al. 2014, ApJL, 781, L23
Wiegelmann, T. 2004, SoPh, 219, 87
Wiegelmann, T., Inhester, B., & Sakurai, T. 2006, SoPh, 233, 215
Xu, Y., Liu, C., Jing, J., & Wang, H. 2012, ApJ, 761, 52
Xu, Z., Yang, K., Guo, Y., et al. 2017, ApJ, 851, 30
Zhong, Z., Guo, Y., Ding, M. D., Fang, C., & Hao, Q. 2019, ApJ, 871, 105